GEOLOGY

Quartz, mica, and amphibole exsolution from majoritic garnet reveals ultra-deep sediment subduction, Appalachian orogen

D. S. Keller[1]* and J. J. Ague[1,2]

Diamond and coesite are classic indicators of ultrahigh-pressure (UHP; ≥100-kilometer depth) metamorphism, but they readily recrystallize during exhumation. Crystallographically oriented pyroxene and amphibole exsolution lamellae in garnet document decomposed supersilicic UHP majoritic garnet originally stable at diamond-grade conditions, but majoritic precursors have only been quantitatively demonstrated in mafic and ultramafic rocks. Moreover, controversy persists regarding which silicates majoritic garnet breakdown produces. We present a method for reconstructing precursor majoritic garnet chemistry in metasedimentary Appalachian gneisses containing garnets preserving concentric zones of crystallographically oriented lamellae including quartz, amphibole, and sodium phlogopite. We link this to novel quartz-garnet crystallographic orientation data. The results reveal majoritic precursors stable at ≥175-kilometer depth and that quartz and mica may exsolve from garnet. Large UHP terranes in the European Caledonides formed during collision of the paleocontinents Baltica and Laurentia; we demonstrate UHP metamorphism from the microcontinent-continent convergence characterizing the contiguous and coeval Appalachian orogen.

INTRODUCTION

The discovery that some continental rocks contain coesite (*1*, *2*) and diamond (*3*, *4*) sparked a paradigm shift in tectonics and metamorphic geology. It is now accepted that continental crustal material may be subducted into the mantle and exhumed, bringing with it otherwise inaccessible information about slab and mantle processes. Studies of ultrahigh-pressure (UHP) rocks and minerals have provided key insights into mantle mineral chemistry (*5*, *6*), diamond formation (*7*), and mantle geodynamics (*8*).

Majoritic garnet, formed by dissolution of pyroxene into the garnet structure at pressures (*P*) of ≥5 GPa, is an important phase in the upper mantle and transition zone (*5*, *9*, *10*). Normal crustal garnets have the general formula $M_3^{VIII}Al_2^{VI}Si_3O_{12}$ (M = Mg^{2+}, Fe^{2+}, Ca^{2+}, and Mn^{2+}; superscript indicates the coordination number). In contrast, majoritic garnet has Si >3 atoms per formula unit (apfu), accommodated by substitutions including $M^{VI} + Si^{VI} = 2\,Al^{VI}$ (*Maj*) (*5*) and $Na^{VIII} + Si^{VI} = Mg^{VIII} + Al^{VI}$ (*Na-Maj*) (*6*). Intact majoritic garnet is rare and only preserved in kimberlite and carbonatite xenoliths, or as inclusions in diamond (*6*, *7*, *10*).

Exhumed, decomposed majoritic garnet may be recognized by diagnostic exsolved precipitates of pyroxene and/or amphibole lamellae (*8*, *11*–*15*). Lamellae have shape-preferred orientation (SPO) parallel to $<111>_{garnet}$, the axis connecting the octahedral sites holding Si^{VI} and Mg^{VI} in majoritic garnet, and preserve crystallographic orientation relationships (CORs) with host garnet (*15*). These relationships are indicative of preferred low-energy alignments formed during precipitation (*16*). Pyroxene and amphibole lamellae compositions and proportions have been used to calculate majoritic precursor chemistry and identify UHP rocks from the diamond stability field (Fig. 1) (*8*, *11*, *12*, *14*).

Quartz lamellae oriented along $<111>_{garnet}$ are known from only two localities, both of which are diamond bearing: the metasedimentary Greek Rhodope (*17*) and eclogites from the kimberlites of Yakutia (*18*). These examples are interpreted as precipitates from majoritic garnet because the precursor garnet would have Si >3 apfu. However, because no COR have been shown for quartz lamellae and calculated precursors are not stoichiometric majoritic garnet (*18*), the precipitate hypothesis remains controversial.

Nonsilicate minerals also form lamellae along $<111>_{garnet}$, including rutile, ilmenite, and apatite (Fig. 1). There is strong evidence that these lamellae precipitate from HP and/or high-temperature (U)HP/(U)HT garnet because they constitute components substituted in garnet at these conditions (e.g., TiO_2 and P_2O_5) (*19*–*21*) and preserve COR with garnet (*16*, *22*).

Lamellae types form characteristic groupings on a *P*-*T* plot (Fig. 1). Rutile has the largest *P*-*T* range, and quartz has the smallest. Of particular significance is that pyroxene, amphibole, or quartz lamellae are only found in rocks formed at ≥~5 GPa, the threshold for majorite-type substitutions. This strongly suggests that these silicate lamellae, including quartz, are UHP petrogenetic indicators.

Dozens of UHP localities are recognized worldwide (*23*) but conspicuously not in continental North America. The Appalachians are now known to contain HP granulites (HPGs) (*24*), indicating similarities to the contemporaneous and formerly laterally contiguous European Caledonides, host to expansive tracts of HPG and UHP rocks (*2*, *8*, *23*). Ultrahigh-temperature (UHT) metapelites are found with HPG rocks in the Brimfield Schist of the Central Maine Terrane (CMT) (*25*, *26*).

RESULTS

Samples

We study ~1050°C garnet-sillimanite-K-feldspar-biotite-quartz gneiss from the Brimfield Schist HPG-UHT field area (*24*, *25*), located within one of several westward-dipping thrust fault-bound slices in the southern CMT. The rocks are highly aluminous (up to ~40 vol%

[1]Department of Geology and Geophysics, Yale University, PO Box 208109, New Haven, CT 06520-8109, USA. [2]Yale Peabody Museum of Natural History, Yale University, New Haven, CT 06511, USA.
*Corresponding author. Email: duncan.keller@yale.edu

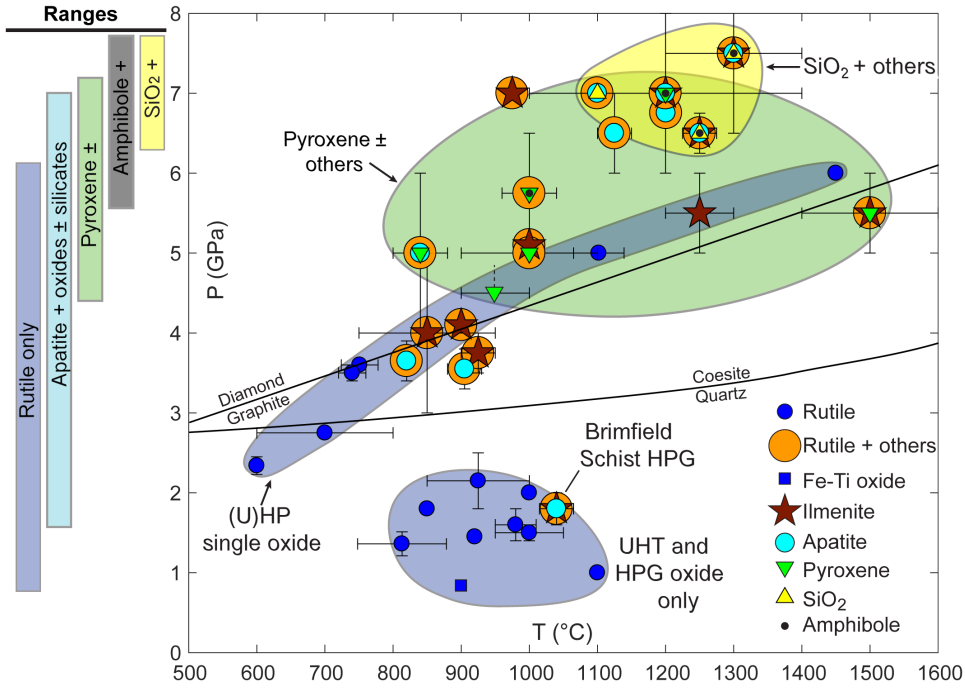

Fig. 1. Lamellae types in garnet as functions of pressure and temperature. Quartz lamellae oriented along <111>$_{garnet}$ are only recognized in metasediments from the Greek Rhodope and eclogite xenoliths in the kimberlite pipes of Yakutia, Russia, both diamondiferous. References are given in Materials and Methods.

garnet and ~30 vol% Al_2SiO_5) and are inferred to have metasedimentary, likely metapelitic, protoliths. Sillimanite pseudomorphs after kyanite are widespread in the field area (*26*), and some samples preserve matrix kyanite. Metamorphism occurred during the Acadian and Neoacadian orogenies ~360 to ~420 Ma (see Materials and Methods for geologic history). The gneiss crops out ~35 km west of the Avalonia-Composite Laurentia subduction suture (fig. S1) as blocks of tens of meters in size within quartzofeldspathic gneiss and amphibolite as part of a ramp-flat sequence which contains ultramafic mélange including hornblende-spinel cumulate blocks in a chloritic, amphibole-bearing matrix (fig. S2). The field area has a complex history involving granulite (~750°C) and amphibolite facies (~575°C) overprints that produced a number of post-peak phases including cordierite and spinel (*25*). The rocks of this study were almost certainly affected by these events, but the macroscopic mineralogical changes appear to have been relatively minor, primarily the pseudomorphic conversion of kyanite to sillimanite, alteration of matrix rutile to ilmenite, and alteration of garnet to biotite (or other hydrous phases) and rutile to ilmenite along cracks in garnet. The limited retrogression likely reflects limited post-peak fluid or melt infiltration. However, preservation of microdiamond and coesite is extremely unlikely given the multistage metamorphic history of the samples.

Garnet contains widespread needle- and plate-shaped lamellae with SPO parallel to <111>$_{garnet}$ (Figs. 2 and 3). Up to three concentric zones distinguished by different lamellae assemblages are present, an extraordinary and hitherto unreported texture (Fig. 2A). The core zone has lamellae of rutile, ilmenite, apatite, and quartz (Fig. 3, B to E), as well as talc and nonlamellar decrepitated inclusions that we infer to be crystallized fluid or hydrous melt (carbonate ± mica ± oxides ± quartz ± graphite) (Figs. 2, B and C, and 3H). The mantle zone has lamellae of quartz, decrepitated mica + quartz ± rutile composites (Fig. 3, F and G), minor rutile, and rare apatite and ilmenite. The outer ring zone has lamellae of rutile, ilmenite, apatite, quartz, orthoamphibole, clinoamphibole (hornblende), talc, Na-phlogopite (aspidolite), and phlogopite (Fig. 3, A and I, and tables S2 and S3), as well as decrepitated inclusions similar to those in cores. Some outer ring lamellae comprise exotic combinations of amphibole, Na-phlogopite, phlogopite, and quartz ± apatite and rutile (Fig. 3, A and I). Quartz is typically the dominant lamellae phase in all zones (Fig. 2, B and C). The core lamellae assemblage (including decrepitated inclusions) is only shared with garnet in diamondiferous eclogite xenoliths from Yakutia (*18*), whereas the mantle and outer ring assemblages are unique. Representative estimates of quartz lamellae content for cores range between ~0.4 and ~1.0 vol% (Materials and Methods).

Coesite and microdiamond are unlikely to have survived the multistage metamorphic history of the Brimfield Schist. This is probably why neither of these UHP phases have been found in our Raman investigations thus far (Materials and Methods). However, relics of coesite and diamond may remain. For example, some quartz lamellae have monoclinic shapes (fig. S4, A and B), suggesting that they precipitated as coesite [e.g., (*18*)]. Furthermore, equant to cuboid graphite crystals that potentially represent former microdiamond are found in nonlamellar inclusions in the garnet that we infer to be former fluid or hydrous melt inclusions; these now contain mostly hydrous and/or carbonate phases (fig. S4C).

CORs and the precipitation hypothesis

We gathered COR data to test the lamellae precipitation hypothesis. Strongly developed apatite, ilmenite, and rutile COR have been demonstrated for these garnets (*16*). Here, we present the first large COR dataset for quartz in garnet from any locality (n = 268). These new data show that quartz has the same dominant COR as ilmenite: a-axis quartz//<111>$_{garnet}$ (± 5°) (Fig. 2D, fig. S3, and table S1) (*16*). For quartz, this COR aligns rows of Si atoms with the garnet octahedral

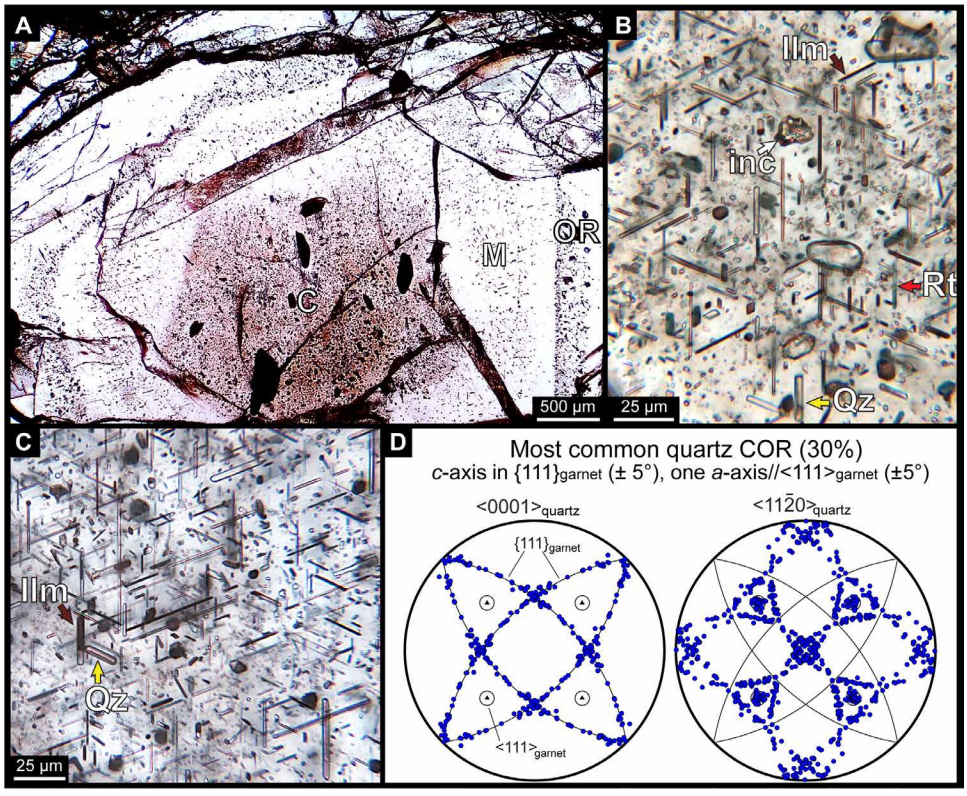

Fig. 2. Garnet textures and quartz COR. Mineral abbreviations follow (*56*) except for inc (crystallized fluid or hydrous melt inclusion). (**A**) Sample 341B-1 showing the diagnostic core, mantle, and outer ring zones. (**B**) Vertically integrated core zone photomicrograph of a 45-µm-thick thin section (58A-8). (**C**) Vertically integrated core zone photomicrograph of a 200-µm-thick section (374A-1). (**D**) The dominant COR for quartz lamellae in garnet measured in the Connecticut samples (symmetrized, antipodal, upper hemisphere, equal angle pole figures).

sites where Si^{VI} substitutes in majoritic garnet. Other quartz CORs are also present, including *c*-axis in $\{111\}_{garnet}$ (± 5°) and *c*-axis//$<100>_{garnet}$ (± 15°), with one *a*-axis//$<100>_{garnet}$ (± 15°) (table S1). Quartz rarely aligns *c*-axis//$<111>_{garnet}$, a COR common for apatite and ilmenite and rare for rutile. Overall, 72% of quartz lamellae have COR, comparable to results for rutile (*16*). It is possible that decrepitation of fluid or hydrous melt inclusions created dislocations, facilitating precipitation (*27*) by heterogeneous nucleation or disrupting the garnet structure post precipitation. These processes could lower COR prevalence. Furthermore, as pointed out above, some quartz lamellae may have precipitated as coesite (fig. S4). These would have formed COR as coesite and not have α-quartz COR upon inversion.

Notably, electron probe microanalyzer (EPMA) spot analyses of garnet show very little TiO_2, and commonly it is below detection limits (table S2). This is quite unusual for garnet in high-grade rocks [e.g., (*27*)] and strongly suggests that Ti was nearly quantitatively removed from the garnet structure by precipitation of rutile- and ilmenite-bearing lamellae.

We conclude that lamellae are exsolved precipitates based on several lines of evidence. Lamellae components are plausibly soluble in the host garnet as constrained by experimental and natural samples (*5*, *20*). Moreover, lamellae SPO is largely restricted to <111>, which connects the octahedral site in garnet where crucial lamellae nutrients substitute. Preservation of COR indicates that lamellae formed preferred relationships with the host, and shared COR between different lamellae minerals in the same garnet is robust evidence for precipitation (*16*). Particularly, quartz lamellae share a dominant COR with ilmenite, demonstrating COR controls at the crystal system level (*16*). This consistency would not be expected if lamellae were the product of, for example, external emplacement.

Some non-exsolution hypotheses for producing lamellae have been proposed, including overgrowth of lamellae by garnet, oriented lamellae attachment to garnet growth faces, various forms of epitaxial intergrowths, and cleaving of garnet followed by infiltration of fluid or melt from which lamellae grew (*16*, *22*). However, despite more than a half century of experimental observations and more than two centuries of studies of natural garnet, we are not aware of examples of oriented lamellae attached to or protruding from garnet growth faces, severely complicating any sort of oriented attachment or garnet-lamellae cogrowth hypothesis. Furthermore, hypotheses involving cleavage are precluded by the fact that garnet lacks cleavage. Detailed discussions of these various lamellae formation hypotheses are given in (*22*) and (*16*).

Alternatively, if lamellae were recrystallization products of pre-existing inclusions, they would be expected to have roughly equant or spherical shapes, which minimize surface area–to–volume ratios and interfacial free energy. This is in strong contrast to the observed highly anisotropic needle and plate morphologies. Needles and plates are hallmarks of precipitation because they minimize lattice strains with the host (*28*), such as in Widmanstätten patterns (*16*).

Last, we note that the quartz lamellae described here are unrelated to the somewhat irregular, elongated quartz grains found in garnets with textural sector zonation formed by epitactic, highly overstepped growth (*29*). This quartz is elongated roughly perpendicular

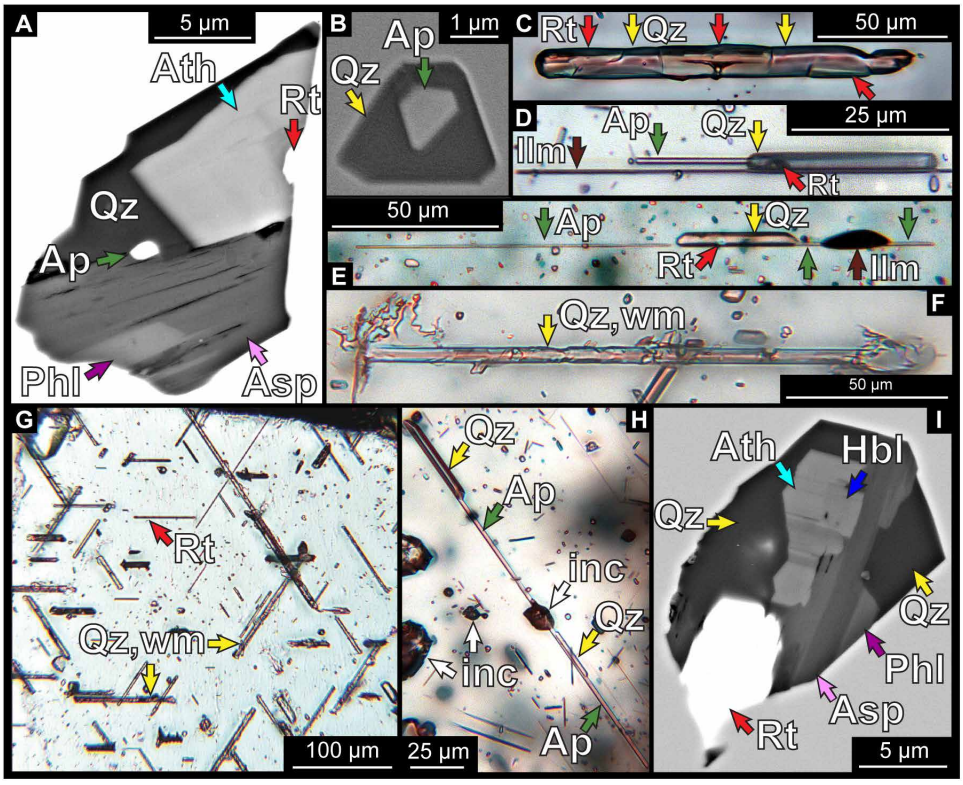

Fig. 3. Composite lamellae. Mineral abbreviations follow (*56*) except for inc (crystallized fluid or hydrous melt inclusion) and wm (white mica). (**A**) Multisilicate lamella needle cross-section in the outer ring zone. (**B**) Crystallographically oriented apatite core in quartz lamella cross-section. (**C**) Rutile-quartz needle. (**D**) Polymineralic core zone needle. (**E**) Polymineralic core zone needle. (**F**) Mantle zone quartz-mica needle (decrepitated). (**G**) Mantle zone assemblage. (**H**) Quartz and apatite composite transecting a crystallized fluid or hydrous melt inclusion. (**I**) Multisilicate lamella needle cross-section in the outer ring zone. Note the presence of two amphiboles and Na-phlogopite (aspidolite).

to growth faces and has no quartz-garnet COR and no SPO parallel to $<111>_{garnet}$ (*22*, *29*).

Majoritic garnet and precursor garnet chemistry

If lamellae precipitated from garnet, then precursor garnet composition may be calculated (*8*, *11*, *12*, *14*) using reintegrated chemical analyses of garnet and lamellae (Materials and Methods). However, because some lamellae phases such as rutile and quartz cannot precipitate stoichiometrically from garnet, reintegration does not produce a stoichiometric garnet formula for some lamellae suites. This complication requires a new approach to study the viability of reintegration, especially for quartz lamellae, which would demonstrate UHP majoritic garnet if successfully reintegrated.

Majoritic garnet compositions vary by rock type. Experimental and natural samples show that garnets in ultramafic bulk compositions are characterized by the *Maj* substitution, garnets in metasedimentary bulk compositions are characterized by *Na-Maj*, and eclogites are characterized by either or a combination (*9*, *10*) (Fig. 4a). Plotting Si + Ti + P against Al + Cr + Fe^{3+} + M^{2+} shows that the trend defined by metasedimentary majoritic garnets is distinct from the ultramafic trend because *Na-Maj* does not balance Si^{VI} with M^{VI}. The observed trend's −1.93 slope is close to the expected −2.0 for the *Na-Maj* substitution but is slightly larger indicating some *Maj* component (Fig. 4A).

EPMA measurements of garnet + lamellae using wide beam grids of varying scales in each garnet zone (Materials and Methods) show M^{VI}-deficient compositions, consistent with the metasedimentary trend (Fig. 4A and Table 1). When Na is included, however, grid results fall close to but below stoichiometric majorite (Fig. 4B), because they have underfilled dodecahedral sites lacking significant Na as well as Al^{IV} or overfilled octahedral sites (Table 1). These results are similar to those for quartz lamellae–bearing eclogite from Yakutia, which has Na-deficient calculated precursor compositions, whereas unexsolved garnets from the same kimberlites show high Na_2O contents (fig. S5 and Materials and Methods) (*30*). Furthermore, loss of Na associated with rutile and apatite precipitation has been documented in diamondiferous UHP garnet from the Saxonian Erzgebirge [Fig. 7 of (*27*)]. Areas in garnet lacking precipitates have elevated Na, Ti, and P contents, whereas precipitate-bearing areas are depleted in these elements. Evidently, then, Na becomes uncoupled to Ti and P during precipitation and diffuses rapidly enough to leave the garnet structure (*27*). These examples demonstrate that UHP garnet breakdown was accompanied by open-system precipitation (OSP) (*22*) involving Na loss and that previous precursor calculations may have produced nonstoichiometric results because open-system behavior was unaccounted for.

Consequently, we present a method for reconstructing garnet precursor compositions using mass balance based on the observed majorite substitution vectors *Na-Maj* (Na^{VIII} + Si^{VI} = M^{VIII} + Al^{VI}) and *Maj* (M^{VI} + Si^{VI} = $2Al^{VI}$) (Fig. 4A). This requires a geochemical reference frame [e.g., (*31*)]. M^{VIII} cations are clearly unsuitable. For example, Mg will have a characteristic $2\sqrt{D_{Mg}t}$ length scale of several millimeters for 10^6 years at 1000°C (*32*), as evidenced by completely flat Mg profiles (fig. S6). More work is needed to characterize Al

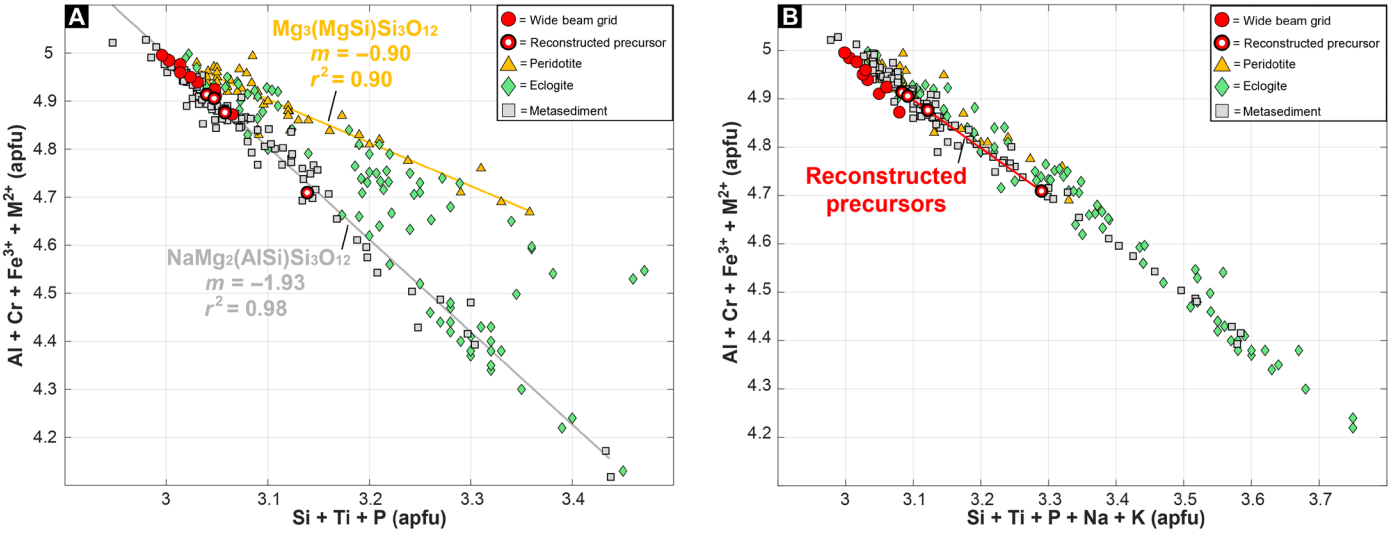

Fig. 4. Compositional trends in natural and synthetic majoritic garnets. (**A**) Majoritic substitutions not including Na + K. r^2, correlation coefficient. (**B**) Majoritic substitutions including Na + K plotted following the method in (*9*) with P included to accommodate a range of bulk compositions and the garnets of this study. References are given in Materials and Methods.

diffusion but, using Cr^{3+} as a proxy, the diffusion coefficient D_{Al} is likely to be only 0.5 to 1.5 $\log_{10}$ units slower than M^{VIII} cations (*33*). Aluminum profiles in garnet are flat and, thus, qualitatively consistent with appreciable Al diffusivity (fig. S6). Sodium diffusion coefficients are not well known, but natural garnet records substantial mobility when lamellae precipitate (*27*), and the measured Na contents in garnet for this study fall within a narrow range (table S2). In sharp contrast, Si^{IV} diffusion in nesosilicates is extremely slow. For forsterite, $D_{Si^{IV}}$ is 10^4 to 10^5 times smaller than for garnet M^{VIII} cations (*34*). In our rocks, radial Si^{IV} growth zonation is retained in a mapped garnet preserving all three lamellae zones (fig. S6), indicating that Si^{IV} has extremely low mobility, even at the >1000°C conditions of metamorphism. Phosphorus and Si largely covary on the tetrahedral sites, and the amount of variation is at most a few tenths of a weight % (wt %) (fig. S6 and table S2). We note that slow diffusion of majorite component also entails sluggish diffusion of coupled Al (*35*). However, once quartz- and Ti-bearing lamellae begin to form, the remaining garnet composition becomes more aluminous and, therefore, D_{Al} is likely to increase, as exemplified by documented cases of pyroxene exsolution (*8*, *11*, *12*, *14*, *15*).

Thus, we use Si as the immobile reference frame, positing that Si^{IV} remained in tetrahedral sites and Si^{VI} deposited locally as quartz lamellae or as silica in other silicate lamellae (e.g., amphiboles) such that Si measured by EPMA grids represents total Si^{IV} + Si^{VI} in precursor garnet. Reconstruction combined the *Na-maj* (−2.0) and *Maj* (−1.0) substitutions proportionately to produce the −1.93 slope defined by experimental results on metasedimentary bulk compositions (Fig. 4A). The *Na-maj* component is adjusted by iteratively adding increments of 0.0001 mol of Na and subtracting 0.0001 mol each of Mg and Al, as set by the exchange vector, for each iteration step. Similarly, the *Maj* component is adjusted by iteratively adding 0.0001 mol of Mg and subtracting 0.0002 mol of Al. The garnet formula is then renormalized to 12 oxygens before the next iteration step. The iterations proceed until the dodecahedral site is filled at 3.0. Furthermore, the octahedral site should sum to 2.0 when the iteration is finished, providing a check on the robustness of the calculation (Table 1). The choice of M^{2+} cation to add or subtract (Mg in this case) is arbitrary.

As the main substitution vectors (*Na-Maj* and *Maj*) are known (Fig. 4A), the primary question surrounding calculation applicability is the Si geochemical reference frame. Tests easily show that reconstructions using Na or Al reference frames fail to converge, producing spurious negative site occupancies. Reconstructions using an M^{2+} reference frame for substitutions dominated by *Maj* produce similar, unacceptable results. Reconstructions using an M^{2+} reference frame can converge if the substitution mechanism is dominantly *Na-Maj*. However, the use of a M^{2+} reference frame is precluded by the high diffusional mobility of these cations as discussed above. In sharp contrast, the Si reference frame produces the garnet site occupancies of 3.0 and 2.0 for dodecahedral and octahedral sites, respectively, and compositions fully consistent with the coupled majorite substitutions.

Reconstructed formulae require modest Al and Mg mass loss (mean −0.68 ± 0.48 wt % 2σ) and Na mass gain (mean +0.44 ± 0.31 wt % 2σ) (Table 1). The reconstructed compositions fall on the expected majorite trend when Na is included (Fig. 4B), demonstrating that the amount of Na restored balances the majoritic substitution preserved by lamellae. Consequently, the majoritic garnet signal is retained by silicate precipitation and may be recovered. Because the ratio of *Na-maj* and *Maj* substitutions is approximate and we have not accounted for other possible substitutions, such as those including K, the formulas should be regarded as semiquantitative. Nonetheless, they firmly establish the operation of majorite-type substitutions consistent with lithological trends (Fig. 4A).

Although we consider open-system behavior as a means to produce quartz lamellae, note that there is no cause for Si to diffuse into garnet (e.g., from the matrix) during lamellae formation. Garnet Si content increases with pressure (*5*, *6*, *10*), and exsolution processes occur during retrogression. This excludes the possibility of Si diffusing into the garnet structure from the matrix to form lamellae because, to do so, the garnet would have to become (more) majoritic. Similar arguments obtain for titanium and phosphorus. Substitutions that

Table 1. Reintegrated precursor garnet chemistry and pressure estimates by zone. Footprints are sums of averaged grid footprints. All Fe as FeO (see Materials and Methods). Pressure calculations used reconstructed compositions and the majorite barometer of (*36*). Note that estimates are insensitive to a range of Fe^{3+} contents. Reintegration procedure is described in the text. Ranges given for reconstructed values represent the 95% confidence bounds for the best-fit slope of −1.93 (Fig. 4A).

Sample	334C-1 Core	334C-1 Core reconstructed	334C-1 Mantle	334C-1 Mantle reconstructed	334C-3a Outer ring	334C-3a Outer ring reconstructed	374A-1 Mantle	374A-1 Mantle reconstructed
Footprint	209,375 μm²		30,625 μm²		15,000 μm²		41,250 μm²	
Si^{IV}	2.986	2.993	2.994	2.994	2.988	2.994	2.982	2.982
P	0.007	0.007	0.006	0.006	0.006	0.006	0.018	0.018
Al^{IV}	0.007				0.006			
ΣTetrahedral	**3.000**	**3.000**	**3.000**	**3.000**	**3.000**	**3.000**	**3.000**	**3.000**
Al	1.977	1.951 (±0.003)	1.990	1.940 (±0.003)	1.959	1.940 (±0.002)	1.959	1.851 (±0.009)
Cr	0.002	0.002	0.001	0.001	0.002	0.002	0.002	0.002
Si^{VI}		0.015	0.023	0.057		0.011	0.064	0.138
Ti	0.025	0.026	0.001	0.001	0.037	0.037	0.001	0.001
M^{2+}		0.007 (±0.003)		0.002 (±0.003)	0.003	0.010 (±0.002)		0.008 (±0.009)
ΣOctahedral	**2.004**	**2.000**	**2.014**	**2.000**	**2.000**	**2.000**	**2.026**	**2.000**
M^{2+}	2.976	2.953 (±0.006)	2.959	2.933 (±0.012)	2.972	2.953 (±0.005)	2.910	2.848 (±0.023)
Na	0.002	0.043 (±0.003)	0.002	0.065 (±0.008)	0.008	0.039 (±0.002)	0.008	0.144 (±0.013)
K		0.001			0.007	0.007	0.007	0.008
Y	0.003	0.003	0.002	0.002	0.002	0.002	0.001	0.001
ΣDodecahedral	**2.981**	**3.000**	**2.964**	**3.000**	**2.989**	**3.000**	**2.927**	**3.000**
Si + Ti + P	3.018	3.040	3.001	3.058	3.031	3.047	3.065	3.139
Si + Ti + P + Na + K	3.02	3.084	3.003	3.122	3.046	3.092	3.08	3.290
Al + Cr + M^{2+}	4.973	4.913	4.95	4.876	4.942	4.905	4.871	4.709
Pressure (Fe^{3+}/**ΣFe = 0.1**)		**6.0**		**6.9**		**5.9**		**8.4**
Pressure (Fe^{3+}/**ΣFe = 0**)		**6.0**		**6.7**		**5.9**		**8.0**

invoke substantial Al^{IV} to force Si off the tetrahedral site to make a silica polymorph are not documented and, in any case, are inapplicable because the garnets have little or no tetrahedral Al (table S2).

We applied a recent majorite barometer (*36*) to estimate formation pressures for each Zone using reconstructed formulae (Table 1). Pressure estimates range from ~6 GPa for core and outer ring zones to ~7 to 8.5 GPa for mantle zones.

Majoritic lamellae

Precursor majoritic garnet is also fingerprinted by talc, amphibole, and mica lamellae. Each of these minerals may be formed from majorite components and water ± SiO_2

$$\underset{\text{Majorite}}{7\,Mg_3[MgSi]Si_3O_{12}} + 4\,H_2O + 4\,SiO_2 = \underset{\text{anthophyllite}}{4\,Mg_7Si_8O_{22}(OH)_2} \quad (1)$$

$$\underset{\text{Majorite}}{3\,Mg_3[MgSi]Si_3O_{12}} + 4\,H_2O + 4\,SiO_2 = \underset{\text{talc}}{4\,Mg_3Si_4O_{10}(OH)_2} \quad (2)$$

$$\underset{\text{Majorite}}{Mg_3[MgSi]Si_3O_{12}} + 4\,\underset{\text{Na-majorite}}{NaMg_2[AlSi]Si_3O_{12}} + 4\,H_2O = 4\,\underset{\text{Aspidolite (Na-phlogopite)}}{NaMg_3AlSi_3O_{10}(OH)_2} + 8\,SiO_2 \quad (3)$$

$$3\,\underset{\text{Majorite}}{Mg_3[MgSi]Si_3O_{12}} + 4\,\underset{\text{Ca-majorite}}{Ca_2Mg[MgSi]Si_3O_{12}} + 4\,H_2O + 4\,SiO_2 = 4\,\underset{\text{Tremolite}}{Ca_2Mg_5Si_8O_{22}(OH)_2} \quad (4)$$

$$2(Na,K)Mg_2[AlSi]Si_3O_{12} + 2\,H_2O = \underset{\text{Na(K)-majorite}}{} SiO_2 + \underset{\text{Aspidolite-phlogopite}}{(Na,K)Mg_3AlSi_3O_{10}(OH)_2} + \underset{\text{Paragonite-phengite}}{(Na,K)Mg(Al,Si)Si_3O_{10}(OH)_2} \quad (5)$$

Water could be supplied by garnet, which can hold up to ~1000 parts per million of H_2O at UHP conditions (*14*). As these model reactions show, amphibole and mica lamellae (e.g., Fig. 3, A, F, G, and I) could have formed entirely from majoritic garnet components. Some precursor garnet K content, as demonstrated in metasedimentary bulk compositions (*37*), would yield potassic mica. Notably, the assemblages preserved in composite silicate lamellae (e.g., aspidolite + phlogopite + anthophyllite + quartz + rutile + apatite; Fig. 3A) do not correspond to known matrix assemblages in rocks or melt compositions of which we are aware. However, their unique nature can be accounted for by majorite breakdown reactions. We also distinguish mantle zone micaceous lamellae produced by model reactions such as Eq. 5 from needles formed by melt elongation (*26*) because the former rarely contain central rutile and therefore lack an elongation mechanism and, critically, are inconsistent with melt compositions. We speculate that the decrepitation features present around the micaceous lamellae (Fig. 3F) formed when mica precipitates underwent partial melting during exhumation and then locally ruptured the garnet during further decompression [e.g., (*26*)].

The best-fit slope of −1.93 for the metasedimentary trend on Fig. 4A is somewhat greater than the ideal 2.0 for the *Na-Maj* substitution, indicating some (~7%) *Maj* component. As shown in Eqs. 1 and 4 above, *Maj* or the calcium analog (*Ca-Maj*) is required to form amphibole lamellae. Talc formation would also require breakdown of *Maj* component (Eq. 2). The talc- and amphibole-bearing lamellae are the least common ones observed, and this can be accounted for by the dominance of the *Na-Maj* substitution relative to *Maj* or *Ca-Maj*. Hornblende, anthophyllite, and gedrite are grossly inconsistent with the mineral assemblages expected in aluminous metasedimentary gneisses but are fully compatible with the breakdown of majoritic components in garnet. As the amphiboles can precipitate stoichiometrically, or very nearly so, from garnet via the *Maj* and *Ca-Maj* substitutions, they need not have been involved in any OSP processes.

Garnet phosphorus content

Garnet phosphorus content increases at elevated *P-T* conditions (*20*, *38*). Measured (not reconstructed) P_2O_5 in garnet EPMA spot analyses reaches 0.32 wt % in garnet mantle zones commensurate with the highest majorite contents (table S2). Experimental and natural garnets ($n = 32$) containing 0.24 to 0.36 wt % P_2O_5 all equilibrated at ≥2.5 GPa (mean 6.3 GPa, 5.2 to 7.7 GPa 2σ; fig. S8). The quartz lamellae–bearing rocks are phosphorus poor (0.03 to 0.04 wt % bulk rock P_2O_5; Materials and Methods) and, thus, were likely apatite undersaturated with garnet, kyanite, and K-feldspar all competing for phosphorus (*38*). Measured garnet phosphorus contents are therefore lower than would be expected for a phosphate-saturated rock yet still are consistent with equilibration at UHP conditions. We speculate that garnet phosphorus contents would have been considerably higher if the rocks were more phosphorus rich.

High phosphorus contents have been found in non-UHP, spessartine-rich garnets from pegmatites and their orthogneiss host rocks (*39*). These garnets have very low MgO (~0 to 1.5 wt %) and up to 40 wt % MnO (fig. S9), as well as distinctive very low CaO (<0.35 wt %) and little Na_2O. The substitutions producing elevated phosphorus contents in these garnets are not well constrained, although Al^{IV} is present and may be involved, in addition to vacancies or some unidentified light element (*39*). The key point is that none of the substitutions that produce elevated phosphorus at HP or UHP conditions (*38*) have been identified in these non-UHP garnets. Moreover, the rocks have high bulk rock P_2O_5 (up to 1.5 wt %) and can contain Li, Fe, Mn, and Ca phosphates; topaz; lepidolite; amblygonite; beryl; columbite; and/or considerable tourmaline. These bulk compositions are clearly not comparable to the aluminous gneisses we study.

In summary, the main characteristics of the pegmatite and (meta)igneous spessartine garnets are: very low Mg and Ca, very high Mn, ubiquitous presence of Al^{IV}, and common association with exotic pegmatitic minerals. These characteristics are grossly at variance with the garnets of our study and UHP garnets generally.

Pseudosection results

Pseudosection results for a sample with plentiful quartz lamellae (Fig. 2B) show that corundum, spinel, and/or cordierite stability is predicted below ~3 GPa at relevant ~1050°C temperatures (fig. S7 and Materials and Methods). These minerals are well known from UHT and/or HPG rocks at the locality (*24*–*26*), so their absence in the rocks of this study suggests matrix equilibration at UHP conditions in excess of about 3 GPa. This pressure result holds for a wide range of H_2O activities and even at minimum is still ~2.6 GPa (fig. S7). Furthermore, quartz is not predicted in the matrix assemblage over most of the investigated *P-T* space for this sample and is absent at UHP conditions, further invalidating any possibility of quartz lamellae representing overgrowths by garnet. The pseudosection does predict a small amount (<1 vol%) of jadeite-rich clinopyroxene at UHP conditions, which is not observed. This is likely due to the small amount and/or the strong propensity of jadeite to rapidly revert to sodic feldspar components during retrogression.

DISCUSSION

Majoritic garnet chemistry may be reconstructed quantitatively from lamellae assemblages containing quartz and other minerals such as rutile, ilmenite, apatite, sodic mica, and amphibole. The reconstruction technique detailed here provides a novel method for identifying former majoritic garnet in metasedimentary rocks. Majoritic garnet represents a robust UHP indicator for deeply subducted samples because unlike diamond and coesite, its retrogressed textures still preserve a record of UHP conditions (*8*, *12*–*14*).

Metamorphism at pressures of ≥6 GPa requires protolith subduction to depths of ≥175 km. Zircon ages for the Brimfield Schist lack significant peri-Gondwanan populations, so the aluminous protolith is not metamorphosed basement (Materials and Methods). Instead, the protolith was more likely oceanic sediment or accretionary wedge material subducted preceding the arrival of Avalonia, which returned to the base of the Laurentian margin as a diapir rising from the slab surface (*40*) or exhumed through the subduction channel, potentially aided by slab breakoff during the Avalonian collision (Fig. 5) (*41*). The less dense host quartzofeldspathic gneiss could potentially rise buoyantly, and in the case of diapirism, the diapir could have been largely solid [e.g., (*40*)]. Higher predicted formation pressures and a different lamellae assemblage in garnet mantle zones suggest that majorite substitution zonation records several depth regimes, perhaps reflecting convection within the subduction channel (Fig. 5) (*42*).

Precipitation of lamellae could have occurred in the granulite or perhaps even upper amphibolite facies (Fig. 4), given that it is necessarily a retrogressive texture and that only α-quartz CORs are

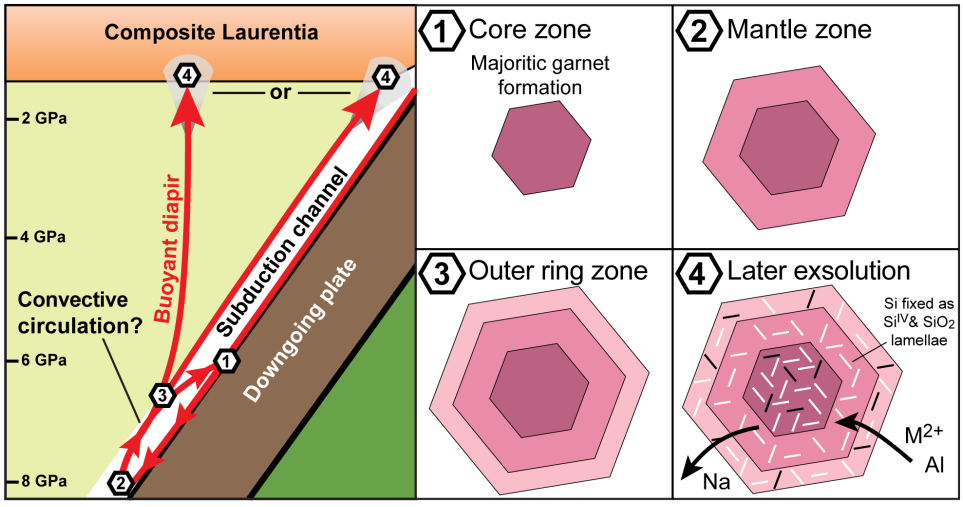

Fig. 5. Garnet growth sequence and tectonic sketch. Convective circulation in the subduction channel after (*42*) and buoyant diapirism after (*40*). Stage 4 could occur along a range of retrograde granulite or perhaps upper amphibolite facies conditions.

observed (Fig. 2D). Amphibole and talc lamellae may have originated as pyroxenes and scavenged H_2O released from garnet during retrogression [e.g., (*14*)], or formed directly by reactions 1 to 5. No quartz or apatite investigated using Raman spectroscopy preserves evidence for (U)HP conditions, fully consistent with the interpretation that the lamellae must have precipitated during retrogression.

Rocks deeply subducted during Pangaea assembly are now known from both sides of the Acadian-Caledonian orogenic belt (*2*, *23*). The Appalachian UHP rocks are the first known from peri-Gondwanan terranes (and the first recognized in continental North America) and show that deep subduction and metamorphism of continental crustal material occurred during microcontinent convergence with the Laurentian margin, reaching a similar grade to that attained in the Baltica-Laurentia continental collision (*8*).

MATERIALS AND METHODS

Regional relations and *P-T* history

The rocks of this study are part of the Brimfield Schist, a unit within the CMT that is bounded by westward-dipping thrust faults (fig. S1). Granulite facies metamorphic conditions for the CMT and neighboring units are well documented (*43*–*45*), and UHT metapelitic gneisses (*25*, *26*), as well as a silica-undersaturated HPG (*24*), have recently been discovered within the Brimfield Schist. Ternary feldspar reintegration thermometry yields an average temperature of ~1050°C for the HPG (*24*), while Zr-in-rutile thermometry and ternary feldspar reintegration thermometry give average temperatures of ~1000°C for the UHT metapelitic gneisses (*25*, *26*). Sillimanite is the primary aluminosilicate phase found in the Brimfield Schist, although rare relict kyanite is present in the rocks of this study, and sillimanite pseudomorphs after kyanite are well known throughout the Brimfield Schist (*26*, *46*, *47*). Brimfield Schist zircon ages do not show a significant peri-Gondwanan signature and record metamorphism between ~360 and ~420 Ma (*48*, *49*).

Evidence for partial melting is preserved in the field as variably developed leucosomes in the gneiss and as leucosomes bordering the blocks in their quartzofeldspathic gneiss and amphibolite host unit (fig. S2). The timing of melting is unconstrained but does not affect our results, as the UHP diagnosis is independent of bulk rock water content (fig. S7).

Several lines of evidence support a prolonged retrograde history for the Brimfield Schist. Granulite facies metamorphism at 700° to 800°C and 0.5 to 0.6 GPa texturally overprints the UHT metapelitic gneisses (*25*). Cross-cutting sillimanite signifies granulite facies conditions in the HPG (*24*). A further kyanite zone overprint is known from cross-cutting kyanite-garnet-quartz-carbonate veins (*50*) and texturally late kyanite (*51*, *52*).

Samples, petrography, and imaging

Rock samples of garnet-sillimanite-biotite gneiss were collected from the field site in northern Connecticut, USA (41.873164°N and 72.275133°W). Petrographic thin and thick sections were made at Yale University. Polishing steps used SiC grit, diamond paste, and lastly, 0.05 μm colloidal silica suspension. Lamellae selection for electron backscatter diffraction (EBSD) analysis followed the procedure in (*16*), with lamellae with clear needle or plate forms and an orientation along $<111>_{garnet}$ chosen. Lamellae locations were recorded. Vertically integrated thin section images were made using a Leica DMC2900 camera attachment and LASv.4.10 software by manually focusing through the depth of the thin section. The sections for 58A-8 and 374A-1 in Fig. 2 are 45 and 200 μm thick, respectively. All sample numbers begin with the prefix JAQ, which is omitted in figures and tables for brevity.

Bulk rock chemistry

Rock bulk chemistry for the pseudosection (sample 58-A) is given in fig. S7. Both x-ray fluorescence analyses for major and minor elements and inductively coupled plasma mass spectrometry analyses for trace elements were performed by SGS Mineral Services. The P_2O_5 contents for representative samples 58A and 334C are 0.04 and 0.03 wt %, respectively.

Pseudosection analysis

Pseudosection calculations (fig. S7) were done in the system Na_2O–CaO–K_2O–FeO–MgO–Al_2O_3–SiO_2–H_2O–TiO_2–O_2

(NCKFMASHTO) using the Theriak-Domino software package (*53*) together with the thermodynamic database of (*54*). Activity models follow the usage of (*23*) except for clinopyroxene, which is from (*55*). The rocks contain graphite and pyrrhotite, and garnet has little or no Fe^{3+} detectable by EPMA (see "Mineral chemistry" section). Consequently, molar $Fe^{3+}/(Fe^{2+} + Fe^{3+})$ was set to the low value of 0.01. Increasing this to as much as 0.1 has little impact on the phase relations relevant for our study. Mineral abbreviations used in pseudosections and figure captions follow (*56*).

Mineral chemistry

Quantitative mineral chemistry analyses and backscattered electron imaging were done using a JEOL JXA-8530F field emission gun EPMA in the Yale University Department of Geology and Geophysics. Garnet unknowns and standards were coated in the same carbon coat application to standardize coat thickness. Kakanui garnet was used as a garnet standard for Si, Al, Ca, and Mg because of its well-characterized ternary composition (*57*). Spessartine was used as the Mn standard and almandine as the Fe standard.

Wavelength-dispersive spectroscopy was used in all runs with natural and synthetic standards and off-peak background corrections. Operating conditions were 15 kV of accelerating voltage and 10.8 mm of working distance with a focused beam. Beam current was 5 nA for apatite, 10 nA for micas and amphiboles, and 20 nA for garnet. Wide beam grids used 25 μm diameter beam spots spaced 25 μm apart. The garnet Si map of fig. S6 used 15 kV of accelerating voltage, 75 nA of beam current, and 200 ms of dwell time with a 1-μm spot size. The garnet P and Al maps of fig. S6 used 15 kV of accelerating voltage, 300 nA of beam current, and 200 ms of dwell time with a 10-μm spot size.

The average structural formula for the garnet analyses sums to eight cations, which implies that garnet Fe^{3+} is minimal (table S2). It would likely have been higher if the samples had reached greater depths (*36*, *58*).

Raman spectroscopy

Raman spectra were taken using a HORIBA-Jobin Yvon HR-800 Raman microscope at Yale University. The instrument uses a 50-mW green laser (532 nm) with a grating of 1800 lines/mm and was calibrated using a Si wafer.

EBSD analyses

EBSD analyses followed the methods in (*16*). Analyses were performed using a Phillips XL30 Environmental Scanning Electron Microscope at Yale University and Oxford Instruments HKL Channel 5 Flamenco software. Analytical conditions were the following: 1×10^{-4} Pa of minimum vacuum strength, 20 mm of working distance, 70° sample tilt, 15 kV of accelerating voltage, ~2 nA of beam current, and beam spot size of 5 (allowing for analysis of lamellae with a diameter of~ ≥1 to 2 μm). Before analyses, backgrounds were acquired in the polygranular rock matrix with 150 to 200 ms timing per frame and 2 × 2 binning. Multiple spot analyses of host garnet were collected for each grain to ensure that garnet hosts were single crystals. Band detection limits were 5 (min) and 6 (max), and only analyses with a mean angular deviation of <1 were considered.

Quartz lamellae volume estimation

Vertically integrated images of thin- and thick-section core zones were taken with the Leica DMC2900 camera attachment and LASv.4.10 software. These images have a scale calibrated to the microscope objective used while acquiring the image. Thin sections cut perpendicular to garnet <111> were selected. Using measuring tools in the Leica Application Suite software, quartz needles were measured for diameter and length, which were used to calculate the volume of each quartz needle assuming a cylindrical shape. Because the sections are viewed along <111>, lamellae are foreshortened because of their dip angles of 35.26°. To correct for this, we multiplied measured lamellae length by 1/cos(35.26°). The vertically integrated images do not show the length of lamellae parallel to the <111> coming out of the image, and consequently, SiO_2 estimates are minima because this direction should account for ~25% of all lamellae. The measured quartz mode for sample 58A-8 (30,000 μm^2) is 0.46 vol%, and the corrected is 0.77 vol%. The measured quartz mode for sample 374B-1 (71,780 μm^2) is 0.25 vol%, and the corrected is 0.31 vol%. These increase to 1.03 and 0.41 vol% if the additional inferred ~25% of the lamellae parallel to <111> are included.

COR categories

Determination of COR types followed the methods in (*16*). The primary search criterion for COR was small angular deviations from major garnet structural features (e.g., <111> and {111}). The proportion of quartz with a prominent COR for rutile, *c*-axis within a 28.5° ± 2.5° cone around $<111>_{garnet}$, is also reported (table S1). Reporting results of the same COR search for each mineral allows for better standardization of COR selection methodology. The most common CORs for each investigated lamellae mineral are shown in fig. S3.

We found only α-quartz-garnet COR, which indicates that most of the SiO_2 precipitated as α-quartz. It is possible that some of this inverted to β-quartz and then back to α-quartz during the retrograde history. It has been shown, however, that in this case neither the *a*-axis nor the *c*-axis change position during the α → β and β → α transformations (*59*).

Figure 1 data sources

Occurrences of lamellae in garnet plotted in Fig. 1 were gathered from the literature from the following references: (*8*, *11*, *12*, *14*, *17*, *18*, *24*, *60*–*99*). Only instances of lamellae oriented along $<111>_{garnet}$ from rocks for which *P-T* estimates are available were used.

Precursor majorite reconstruction

Garnet + lamellae compositions were measured by EPMA wide beam grids with a spot size of 25 μm. Wide beam grid results are given in Table 1. Precursor compositions were calculated from these grids using a MATLAB code available from the authors by request. Results are identical if the $Na_2Mg[Si_2]Si_3O_{12}$ end-member (*100*) is used to represent *Na-maj*, and exchange vectors are adjusted accordingly.

The precursor reconstruction method was tested using exsolved and unexsolved eclogite garnet examples from Yakutia. Sample UV662/11 garnet illustrated in Fig. 4 (A and B) in (*18*) contains needle-shaped quartz lamellae, as well as coesite and monoclinic quartz paramorphs, after coesite. The lamellae of our study appear texturally identical, so UV662/11 is an excellent basis for comparison. The reintegrated garnet + lamellae composition (*18*) is Na deficient relative to unexsolved majoritic garnet (*30*). This is confirmed in fig. S5A, which shows that the garnet plots near the *Na-maj* trend. In fig. S5B, which includes Na content, the garnet falls off the general

majorite trend due primarily to the Na deficiency. The reconstruction produces majoritic garnet with perfect site occupancies and only requires small changes in mass. All of these traits are comparable to the garnets in our study.

Percentage mass change values for Na_2O, MgO, and Al_2O_3 were calculated using the mass balance equation [e.g., (*31*)]

$$\frac{m'_j - m^\circ_j}{m^\circ_j} - \frac{m'_j}{m^\circ_j} - 1 = \frac{(C^\circ_i)}{C'_i}\frac{C'_j}{C^\circ_j}$$

in which m is mass, C is concentration, ° denotes precursor state, $'$ denotes final state, and the subscripts i and j denote the reference species (Si) and a mobile species, respectively. The percentage values change somewhat depending on which M^{2+} cation is used for majorite reconstruction, but the differences are small and do not affect our conclusions. We clarify that we use the term exsolution in a general way to refer to phase separation (or unmixing) by precipitation.

Figure 4 data sources

Compositional data for natural and synthetic majoritic garnets plotted in Fig. 4 were gathered from the literature from the following references: (*37*, *101*–*107*). Data from (*37*) with wt % totals >102% or <98% were excluded.

SUPPLEMENTARY MATERIALS

Supplementary material for this article is available at http://advances.sciencemag.org/cgi/content/full/6/11/eaay5178/DC1

Fig. S1. Geologic setting and regional relations.
Fig. S2. Geologic map and cross-section of field area.
Fig. S3. Dominant COR for lamellae minerals in the garnets of this study.
Fig. S4. Inferred paramorphs after UHP indicator minerals.
Fig. S5. Compositional trends in natural and synthetic majoritic garnets with reconstructed and natural examples from Yakutia and the rocks of this study.
Fig. S6. Elemental zonation in sample 334C-1.
Fig. S7. Thermodynamic pseudosections for sample 58A.
Fig. S8. Equilibration pressures of natural and experimental synthetic garnet with 0.24 to 0.36 wt % P_2O_5.
Fig. S9. Major element trends in high-phosphorus garnets.
Table S1. Quartz COR and COR for trigonal minerals from (*16*).
Table S2. Garnet chemistry measured by EPMA.
Table S3. Inosilicate lamellae chemistry measured by EPMA.
Table S4. Phyllosilicate, apatite, and carbonate analyses measured by EPMA.
References (*108*–*115*)

REFERENCES AND NOTES

1. C. Chopin, Coesite and pure pyrope in high-grade blueschists of the Western Alps: A first record and some consequences. *Contrib. Mineral. Petrol.* **86**, 107–118 (1984).
2. D. C. Smith, Coesite in clinopyroxene in the Caledonides and its implications for geodynamics. *Nature* **310**, 641–644 (1984).
3. N. V. Sobolev, V. S. Shatsky, Diamond inclusions in garnets from metamorphic rocks: A new environment for diamond formation. *Nature* **343**, 742–746 (1990).
4. L. Nasdala, H.-J. Massonne, Microdiamonds from the Saxonian Erzgebirge, Germany: *In situ* micro-Raman characterization. *Eur. J. Mineral.* **12**, 495–498 (2000).
5. A. E. Ringwood, A. Major, Synthesis of majorite and other high pressure garnets and perovskites. *Earth Planet. Sci. Lett.* **12**, 411–418 (1971).
6. N. V. Sobolev Jr., J. G. Lavrent'ev, Isomorphic sodium admixture in garnets formed at high pressures. *Contrib. Mineral. Petrol.* **31**, 1–12 (1971).
7. B. Harte, Diamond formation in the deep mantle: The record of mineral inclusions and their distribution in relation to mantle dehydration zones. *Mineral. Mag.* **74**, 189–215 (2010).
8. H. L. M. van Roermund, M. R. Drury, Ultra-high pressure (P > 6 GPa) garnet peridotites in Western Norway: Exhumation of mantle rocks from > 185 km depth. *Terra Nova* **10**, 295–301 (1998).
9. E. S. Kiseeva, G. M. Yaxley, A. S. Stepanov, H. Tkalčić, K. D. Litasov, V. S. Kamenetsky, Metapyroxenite in the mantle transition zone revealed from majorite inclusions in diamonds. *Geology* **41**, 883–886 (2013).
10. B. J. Wood, E. S. Kiseeva, A. K. Matzen, Garnet in the Earth's mantle. *Elements* **9**, 421–426 (2013).
11. S. E. Haggerty, V. Sautter, Ultradeep (greater than 300 kilometers), ultramafic upper mantle xenoliths. *Science* **248**, 993–996 (1990).
12. K. Ye, B. Cong, D. Ye, The possible subduction of continental material to depths greater than 200 km. *Nature* **407**, 734–736 (2000).
13. L. F. Dobrzhinetskaya, H. W. Green II, A. P. Renfro, K. N. Bozhilov, D. Spengler, H. L. M. van Roermund, Precipitation of pyroxenes and Mg2SiO4 from majoritic garnet: Simulation of peridotite exhumation from great depth. *Terra Nova* **16**, 325–330 (2004).
14. S. Song, L. Zhang, J. Chen, J. G. Liou, Y. Niu, Sodic amphibole exsolutions in garnet from garnet-peridotite, North Qaidaim UHPM belt, NW China: Implications for ultradeep-origin and hydroxyl defects in mantle garnets. *Am. Mineral.* **90**, 814–820 (2005).
15. H. J. Xu, Y. Wu, Oriented inclusions of pyroxene, amphibole, and rutile in garnet from the Lüliangshan garnet peridotite massif, North Qaidam UHPM belt, NW China: An electron backscatter diffraction study. *J. Metamorph. Geol.* **35**, 1–17 (2017).
16. D. S. Keller, J. J. Ague, Crystallographic and textural evidence for precipitation of rutile, ilmenite, corundum, and apatite lamellae from garnet. *Am. Mineral.* **104**, 980–995 (2019).
17. E. D. Mposkos, D. K. Kostopoulos, Diamond, former coesite and supersilicic garnet in metasedimentary rocks from the Greek Rhodope: A new ultrahigh-pressure metamorphic province established. *Earth Planet. Sci. Lett.* **192**, 497–506 (2001).
18. T. A. Alifirova, L. N. Pokhilenko, A. V. Korsakov, Apatite, SiO2, rutile and orthopyroxene precipitates in minerals of eclogite xenoliths from Yakutian kimberlites, Russia. *Lithos* **226**, 31–49 (2015).
19. W. L. Griffin, Major transformations reveal Earth's deep secrets. *Geology* **36**, 95–96 (2008).
20. J. Hermann, C. J. Spandler, Sediment melts at sub-arc depths: An experimental study. *J. Petrol.* **49**, 717–740 (2008).
21. M. R. Ackerson, E. B. Watson, N. D. Tailby, F. S. Spear, Experimental investigation into the substitution mechanisms and solubility of Ti in garnet. *Am. Mineral.* **102**, 158–172 (2017).
22. A. Proyer, G. Habler, R. Abart, R. Wirth, K. Krenn, G. Hoinkes, TiO_2 exsolution from garnet by open-system precipitation: Evidence from crystallographic and shape preferred orientation of rutile inclusions. *Contrib. Mineral. Petrol.* **166**, 211–234 (2013).
23. J. A. Gilotti, The realm of ultrahigh-pressure metamorphism. *Elements* **9**, 255–260 (2013).
24. D. S. Keller, J. J. Ague, High-pressure granulite facies metamorphism (~1.8 GPa) revealed in silica-undersaturated garnet-spinel-corundum gneiss, Central Maine Terrane, Connecticut, U.S.A. *Am. Mineral.* **103**, 1851–1868 (2018).
25. J. J. Ague, J. O. Eckert Jr., X. Chu, E. F. Baxter, C. P. Chamberlain, Discovery of ultrahigh-temperature metamorphism in the Acadian orogen, Connecticut, USA. *Geology* **41**, 271–274 (2013).
26. J. A. Axler, J. J. Ague, Oriented multiphase needles in garnet from ultrahigh-temperature granulites, Connecticut, U.S.A. *Am. Mineral.* **100**, 2254–2271 (2015).
27. J. A. Axler, J. J. Ague, Exsolution of rutile or apatite precipitates surrounding ruptured inclusions in garnet from UHT and UHP rocks. *J. Metamorph. Geol.* **33**, 829–848 (2015).
28. F. R. N. Nabarro, The strains produced by precipitation in alloys. *Proc. R. Soc. Lond. A* **175**, 519–538 (1940).
29. D. E. Wilbur, J. J. Ague, Chemical disequilibrium during garnet growth: Monte Carlo simulations of natural crystal morphologies. *Geology* **34**, 689–692 (2006).
30. N. V. Sobolev, A. M. Logvinova, D. A. Zedgenizov, Y. V. Seryotkin, E. S. Yefimova, C. Floss, L. A. Taylor, Mineral inclusions in microdiamonds and macrodiamonds from kimberlites of Yakutia: A comparative study. *Lithos* **77**, 225–242 (2004).
31. J. J. Ague, S. Nicolescu, Carbon dioxide released from subduction zones by fluid-mediated reactions. *Nat. Geosci.* **7**, 355–360 (2014).
32. S. Chakraborty, J. Ganguly, Cation diffusion in aluminosilicate garnets: Experimental determination in spessartine-almandine diffusion couples, evaluation of effective binary diffusion coefficients, and applications. *Contrib. Mineral. Petrol.* **111**, 74–86 (1992).
33. W. D. Carlson, Rates and mechanism of Y, REE, and Cr diffusion in garnet. *Am. Mineral.* **97**, 1598–1618 (2012).
34. H. Fei, C. Hegoda, D. Yamazaki, M. Wiedenbeck, H. Yurimoto, S. Shcheka, T. Katsura, High silicon self-diffusion coefficient in dry forsterite. *Earth Planet. Sci. Lett.* **345–348**, 95–103 (2012).
35. W. L. van Mierlo, F. Langenhorst, D. J. Frost, D. C. Rubie, Stagnation of subducting slabs in the transition zone due to slow diffusion in majoritic garnet. *Nat. Geosci.* **6**, 400–403 (2013).
36. R. Tao, Y. Fei, E. S. Bullock, C. Xu, L. Zhang, Experimental investigation of Fe^{3+}-rich majoritic garnet and its effect on majorite geobarometer. *Geochim. Cosmochim. Acta* **225**, 1–16 (2018).
37. D. Grassi, M. W. Schmidt, The melting of carbonated pelites from 70 to 700 km depth. *J. Petrol.* **52**, 765–789 (2011).
38. J. Konzett, From phosphates to silicates and back: An experimental study on the transport and storage of phosphorus in eclogites during uplift and exhumation. *Am. Mineral.* **101**, 1756–1768 (2016).

39. K. Breiter, M. Novák, F. Koller, J. Cempírek, Phosphorus – an omnipresent minor element in garnet of diverse textural types from leucocratic granitic rocks. *Mineral. Petrol.* **85**, 205–221 (2005).
40. B. R. Hacker, P. B. Kelemen, M. D. Behn, Differentiation of the continental crust by relamination. *Earth Planet. Sci. Lett.* **307**, 501–516 (2011).
41. J. H. Davies, F. von Blanckenburg, Slab breakoff: A model of lithosphere detachment and its test in the magmatism and deformation of collisional orogens. *Earth Planet. Sci. Lett.* **129**, 85–102 (1995).
42. J.-L. Li, R. Klemd, J. Gao, T. John, Poly-cyclic metamorphic evolution of eclogite: Evidence for multistage burial–exhumation cycling in a subduction channel. *J. Petrol.* **57**, 119–146 (2016).
43. R. J. Tracy, P. Robinson, A. B. Thompson, Garnet composition and zoning in the determination of temperature and pressure of metamorphism, central Massachusetts. *Am. Mineral.* **61**, 762–775 (1976).
44. P. Robinson, The Bronson Hill anticlinorium and Merrimack synclinorium in central Massachusetts—An Acadian "Pennine zone". *Geol. Soc. Am. Abstr. Programs* **10**, 82 (1978).
45. J. Rodgers, The Merrimack Synclinorium in northeastern Connecticut. *Am. J. Sci.* **281**, 176–186 (1981).
46. J. D. Peper, M. H. Pease Jr., Geologic map of the Westford quadrangle, Connecticut, (U.S. Geol. Survey Quad. Map, **GQ-1214**, 1975).
47. R. J. Fahey, M. H. Pease Jr., Preliminary bedrock geologic map of the South Coventry quadrangle, Tolland County, Connecticut, (U.S. Geol. Survey Open-File Report, 1977), pp. **77-587**.
48. R. P. Wintsch, J. N. Aleinikoff, G. J. Walsh, W. A. Bothner, A. M. Hussey II, C. M. Fanning, SHRIMP U-Pb evidence for a Late Silurian age of metasedimentary rocks in the Merrimack and Putnam-Nashoba terranes, eastern New England. *Am. J. Sci.* **307**, 119–167 (2007).
49. J. A. Axler, PhD thesis, Yale University (2016).
50. J. J. Ague, Deep crustal growth of quartz, kyanite and garnet into large-aperture, fluid-filled fractures, north-eastern Connecticut, USA. *J. Metamorph. Geol.* **13**, 299–314 (1995).
51. J. C. Schumacher, R. Schumacher, P. Robinson, in *Evolution of Metamorphic Belts*, J. S. Daly, R. A. Cliff, B. W. D. Yardley, Eds. (Blackwell Scientific, Boston, 1989), pp. 453–460.
52. J. A. Thomson, A counterclockwise P–T path for anatectic pelites, south-central Massachusetts. *Contrib. Mineral. Petrol.* **141**, 623–641 (2001).
53. C. de Capitani, K. Petrakakis, The computation of equilibrium assemblage diagrams with Theriak/Domino software. *Am. Mineral.* **95**, 1006–1016 (2010).
54. T. J. B. Holland, R. Powell, An improved and extended internally consistent thermodynamic dataset for phases of petrological interest, involving a new equation of state for solids. *J. Metamorph. Geol.* **29**, 333–383 (2011).
55. E. C. R. Green, R. W. White, J. F. A. Diener, R. Powell, T. J. B. Holland, R. M. Palin, Activity–composition relations for the calculation of partial melting equilibria in metabasic rocks. *J. Metamorph. Geol.* **34**, 845–869 (2016).
56. D. L. Whitney, B. W. Evans, Abbreviations for names of rock-forming minerals. *Am. Mineral.* **95**, 185–187 (2010).
57. B. Mason, Eclogitic xenoliths from volcanic breccia at Kakanui, New Zealand. *Contrib. Mineral. Petrol.* **19**, 316–327 (1968).
58. E. S. Kiseeva, D. M. Vasiukov, B. J. Wood, C. McCammon, T. Stachel, M. Bykov, E. Bykova, A. Chumakov, V. Cerantola, J. W. Harris, L. Dubrovinsky, Oxidized iron in garnets from the mantle transition zone. *Nat. Geosci.* **11**, 144–147 (2018).
59. H.-R. Wenk, N. Barton, M. Bortolotti, S. C. Vogel, M. Voltolini, G. E. Lloyd, G. B. Gonzalez, Dauphiné twinning and texture memory in polycrystalline quartz. Part 3: Texture memory during phase transformation. *Phys. Chem. Miner.* **36**, 567–583 (2009).
60. T. A. Alifirova, L. N. Pokhilenko, A. V. Korsakov, Amphibole in exsolution textures of garnet and its connection with fluid-saturated conditions of ancient subduction zones, in *11th International GeoRaman Conference* (15 to 19 June 2014), pp. 5084.
61. H. K. Brueckner, L. G. Medaris, A general model for the intrusion and evolution of 'mantle' garnet peridotites in high-pressure and ultra-high-pressure metamorphic terranes. *J. Metamorph. Geol.* **18**, 123–133 (2000).
62. R. Caby, O. Bruguier, L. Fernandez, D. Hammor, D. Bosch, M. Mechati, R. Laouar, A. Ouabadi, N. Abdallah, C. Douchet, Metamorphic diamonds in a garnet megacryst from the Edough Massif (northeastern Algeria). Recognition and geodynamic consequences. *Tectonophysics* **637**, 341–353 (2014).
63. T. Chapman, G. L. Clarke, N. R. Daczko, S. Piazolo, A. Rajkumar, Orthopyroxene–omphacite- and garnet–omphacite-bearing magmatic assemblages, Breaksea Orthogneiss, New Zealand: Oxidation state controlled by high-*P* oxide fractionation. *Lithos* **216–217**, 1–16 (2015).
64. G. L. Clarke, N. R. Daczko, D. Miescher, Identifying relic igneous garnet and clinopyroxene in eclogite and granulite, Breaksea Orthogneiss, New Zealand. *J. Petrol.* **54**, 1921–1938 (2013).
65. R. A. Cooke, P. J. O'Brien, Resolving the relationship between high *P–T* rocks and gneisses in collisional terranes: An example from the Gföhl gneiss–granulite association in the Moldanubian Zone, Austria. *Lithos* **58**, 33–54 (2001).
66. K. Das, N. Tomioka, S. Bose, J.-i. Ando, On oriented ilmenite needles in garnet porphyroblasts from deep crustal granulites: Implications for fluid evolution and cooling history. *Lithos* **156–159**, 230–240 (2013).
67. S. Dludla, A. P. le Roex, J. J. Gurney, Eclogite xenoliths from the Premier kimberlite, South Africa: Geochemical evidence for a subduction origin. *S. Afr. J. Geol.* **109**, 353–368 (2006).
68. A. T. Fung, S. E. Haggerty, Petrography and mineral compositions of eclogites from the Koidu Kimberlite Complex, Sierra Leone. *J. Geophys. Res.* **100**, 20451–20473 (1995).
69. W. E. Glassley, J. A. Korstgård, K. Sørensen, S. W. Platou, A new UHP metamorphic complex in the ~1.8 Ga Nagssugtoqidian Orogen of West Greenland. *Am. Mineral.* **99**, 1315–1334 (2014).
70. S. L. Hwang, T. F. Yui, H. T. Chu, P. Shen, H. P. Schertl, R. Y. Zhang, J. G. Liou, On the origin of oriented rutile needles in garnet from UHP eclogites. *J. Metamorph. Geol.* **25**, 349–362 (2007).
71. S. Keshav, G. Sen, Majoritic garnets in Hawaiian xenoliths: Preliminary results. *Geophys. Res. Lett.* **28**, 3509–3512 (2001).
72. S. Keshav, G. Sen, D. C. Presnall, Garnet-bearing xenoliths from Salt Lake Crater, Oahu, Hawaii: High-pressure fractional crystallization in the oceanic mantle. *J. Petrol.* **48**, 1681–1724 (2007).
73. R. B. Larsen, E. A. Eide, E. A. J. Burke, Evolution of metamorphic volatiles during exhumation of microdiamond-bearing granulites in the Western Gneiss Region, Norway. *Contrib. Mineral. Petrol.* **133**, 106–121 (1998).
74. S. J. Liu, J. H. Li, M. Santosh, First application of the revised Ti-in-zircon geothermometer to Paleoproterozoic ultrahigh-temperature granulites of Tuguiwula, Inner Mongolia, North China Craton. *Contrib. Mineral. Petrol.* **159**, 225–235 (2010).
75. N. Malaspina, J. Hermann, M. Scambelluri, R. Compagnoni, Multistage metasomatism in ultrahigh-pressure mafic rocks from the North Dabie Complex (China). *Lithos* **90**, 19–42 (2006).
76. H. R. Marschall, A. Kalt, M. Hanel, *P–T* evolution of a Variscan lower-crustal segment: A study of granulites from the Schwarzwald, Germany. *J. Petrol.* **44**, 227–253 (2003).
77. J. H. Marsh, E. D. Kelly, Petrogenetic relations among titanium-rich minerals in an anatectic high-*P* mafic granulite. *J. Metamorph. Geol.* **35**, 717–738 (2017).
78. H.-J. Massonne, T. Fockenberg, Melting of metasedimentary rocks at ultrahigh pressure—Insights from experiments and thermodynamic calculations. *Lithosphere* **4**, 269–285 (2012).
79. Y. O. Mohammad, D. H. Cornell, E. Danielsson, E. A. Hegardt, R. Anczkiewicz, Mg-rich staurolite and kyanite inclusions in metabasic garnet amphibolite from the Swedish Eastern Segment: Evidence for a Mesoproterozoic subduction event. *Eur. J. Mineral.* **23**, 609–631 (2011).
80. M. Obata, Material transfer and local equilibria in a zoned kelyphite from a garnet pyroxenite, Ronda, Spain. *J. Petrol.* **35**, 271–287 (1994).
81. Y. Osanai, N. Nakano, M. Owada, T. N. Nam, T. Miyamoto, N. T. Minh, N. V. Nam, T. V. Tri, Collision zone metamorphism in Vietnam and adjacent South-eastern Asia: Proposition for Trans Vietnam Orogenic Belt. *J. Mineral. Petrol. Sci.* **103**, 226–241 (2008).
82. C. D. Parkinson, Coesite inclusions and prograde compositional zonation of garnet in whiteschist of the HP-UHPM Kokchetav massif, Kazakhstan: A record of progressive UHP metamorphism. *Lithos* **52**, 215–233 (2000).
83. S. C. Patel, S. Ravi, S. S. Thakur, T. K. Rao, K. V. Subbarao, Eclogite xenoliths from Wajrakarur kimberlites, southern India. *Mineral. Petrol.* **88**, 363–380 (2006).
84. A. L. Perchuk, Unusual inclusions in garnet from the diamond-bearing gneiss of the Erzgebirge, Germany. *Geochem. Int.* **46**, 296–303 (2008).
85. M. D. Ruiz-Cruz, C. Sanz de Galdeano, Coesite and diamond inclusions, exsolution microstructures and chemical patterns in ultrahigh pressure garnet from Ceuta (Northern Rif, Spain). *Lithos* **177**, 184–206 (2013).
86. K. Sajeev, T. Kawai, S. Omori, B. F. Windley, S. Maruyama, *P–T* evolution of Glenelg eclogites, NW Scotland: Did they experience ultrahigh-pressure metamorphism? *Lithos* **114**, 473–489 (2010).
87. K. Sajeev, B. F. Windley, J. A. D. Connolly, Y. Kon, Retrogressed eclogite (20 kbar, 1020°C) from the Neoproterozoic Palghat–Cauvery suture zone, southern India. *Precambrian Res.* **171**, 23–36 (2009).
88. K. Sakamaki, Y. Sato, Y. Ogasawara, Hydrous Na-garnet from Garnet Ridge; products of mantle metasomatism underneath the Colorado Plateau. *Prog Earth Planet Sci* **3**, 20 (2016).
89. M. Santosh, T. Tsunogae, J. H. Li, S. J. Liu, Discovery of sapphirine-bearing Mg–Al granulites in the North China Craton: Implications for Paleoproterozoic ultrahigh temperature metamorphism. *Gondwana Res.* **11**, 263–285 (2007).
90. V. Sautter, S. E. Haggerty, S. Field, Ultradeep (>300 Kilometers) ultramafic xenoliths: Petrological evidence from the transition zone. *Science* **252**, 827–830 (1991).
91. B. Schmickler, D. E. Jacob, S. F. Foley, Eclogite xenoliths from the Kuruman kimberlites, South Africa: Geochemical fingerprinting of deep subduction and cumulate processes. *Lithos* **75**, 173–207 (2004).
92. D. R. Snoeyenbos, M. L. Williams, S. Hanmer, Archean high-pressure metamorphism in the western Canadian Shield. *Eur. J. Mineral.* **7**, 1251–1272 (1995).

93. S. Song, L. Zhang, Y. Niu, Ultra-deep origin of garnet peridotite from the North Qaidam ultrahigh-pressure belt, Northern Tibetan Plateau, NW China. *Am. Mineral.* **89**, 1330–1336 (2004).
94. H. Stowell, K. O. Parker, M. Gatewood, A. Tulloch, A. Koenig, Temporal links between pluton emplacement, garnet granulite metamorphism, partial melting and extensional collapse in the lower crust of a Cretaceous magmatic arc, Fiordland, New Zealand. *J. Metamorph. Geol.* **32**, 151–175 (2014).
95. M. P. Terry, P. Robinson, E. J. Krogh Ravna, Kyanite eclogite thermobarometry and evidence for thrusting of UHP over HP metamorphic rocks, Nordøyane, Western Gneiss Region, Norway. *Am. Mineral.* **85**, 1637–1650 (2000).
96. H. L. M. Van Roermund, M. R. Drury, A. Barnhoorn, A. De Ronde, Non-silicate inclusions in garnet from an ultra-deep orogenic peridotite. *Geol. J.* **35**, 209–229 (2000).
97. H. L. M. Van Roermund, M. R. Drury, A. Barnhoorn, A. De Ronde, Relict majoritic garnet microstructures from ultra-deep orogenic peridotites in western Norway. *J. Petrol.* **42**, 117–130 (2001).
98. S. Vrána, Mineral inclusions in pyrope from garnet peridotites, Kolín area, central Czech Republic. *J. Geosci.* **53**, 17–30 (2008).
99. L. Wang, E. J. Essene, Y. Zhang, Mineral inclusions in pyrope crystals from Garnet Ridge, Arizona, USA: Implications for processes in the upper mantle. *Contrib. Mineral. Petrol.* **135**, 164–178 (1999).
100. C. Beyer, D. J. Frost, The depth of sub-lithospheric diamond formation and the redistribution of carbon in the deep mantle. *Earth Planet. Sci. Lett.* **461**, 30–39 (2017).
101. C. H. Wijbrans, A. Rohrbach, S. Klemme, An experimental investigation of the stability of majoritic garnet in the Earth's mantle and an improved majorite geobarometer. *Contrib. Mineral. Petrol.* **171**, 50 (2016).
102. E. Auzanneau, M. W. Schmidt, D. Vielzeuf, J. A. D. Connolly, Titanium in phengite: A geobarometer for high temperature eclogites. *Contrib. Mineral. Petrol.* **159**, 1–24 (2010).
103. S. Ono, Stability limits of hydrous minerals in sediment and mid-ocean ridge basalt compositions: Implications for water transport in subduction zones. *J. Geophys. Res.* **103**, 18253–18267 (1998).
104. K. D. Collerson, Q. Williams, B. S. Kamber, S. Omori, H. Arai, E. Ohtani, Majoritic garnet: A new approach to pressure estimation of shock events in meteorites and the encapsulation of sub-lithospheric inclusions in diamond. *Geochim. Cosmochim. Acta* **74**, 5939–5957 (2010).
105. C. Spandler, G. Yaxley, D. H. Green, D. Scott, Experimental phase and melting relations of metapelite in the upper mantle: Implications for the petrogenesis of intraplate magmas. *Contrib. Mineral. Petrol.* **160**, 569–589 (2010).
106. T. Irifune, A. E. Ringwood, W. O. Hibberson, Subduction of continental crust and terrigenous and pelagic sediments: An experimental study. *Earth Planet. Sci. Lett.* **126**, 351–368 (1994).
107. E. S. Kiseeva, K. D. Litasov, G. M. Yaxley, E. Ohtani, V. S. Kamenetsky, Melting and phase relations of carbonated eclogite at 9–21 GPa and the petrogenesis of alkali-rich melts in the deep mantle. *J. Petrol.* **54**, 1555–1583 (2013).
108. R. N. Thompson, Is upper-mantle phosphorus contained in sodic garnet? *Earth Planet. Sci. Lett.* **26**, 417–424 (1975).
109. J. Konzett, D. J. Frost, The high *P–T* stability of hydroxyl-apatite in natural and simplified MORB—An experimental study to 15 GPa with implications for transport and storage of phosphorus and halogens in subduction zones. *J. Petrol.* **50**, 2043–2062 (2009).
110. J. Konzett, D. Rhede, D. J. Frost, The high PT stability of apatite and Cl partitioning between apatite and hydrous potassic phases in peridotite: An experimental study to 19 GPa with implications for the transport of P, Cl and K in the upper mantle. *Contrib. Mineral. Petrol.* **163**, 277–296 (2012).
111. Q. Qian, J. Hermann, Partial melting of lower crust at 10–15 kbar: Constraints on adakite and TTG formation. *Contrib. Mineral. Petrol.* **165**, 1195–1224 (2013).
112. E. S. Kiseeva, G. M. Yaxley, J. Hermann, K. D. Litasov, A. Rosenthal, V. S. Kamenetsky, An experimental study of carbonated eclogite at 3.5–5.5 GPa—Implications for silicate and carbonate metasomatism in the cratonic mantle. *J. Petrol.* **53**, 727–759 (2012).
113. J. Hermann, D. Rubatto, Subduction of continental crust to mantle depth: Geochemistry of ultrahigh-pressure rocks, in *Treatise on Geochemistry*, H. D. Holland, K. Turekian, Eds. (Elsevier, ed. 2, 2014), pp. 309–340.
114. G. Habler, T. Griffiths, in *Mineral Reaction Kinetics: Microstructures, Textures, Chemical and Isotopic Signatures*, W. Heinrich, R. Abart, Eds. (The Mineralogical Society of Great Britain & Ireland, 2017), pp. 541–585.
115. T. A. Griffiths, G. Habler, R. Abart, Crystallographic orientation relationships in host–inclusion systems: New insights from large EBSD data sets. *Am. Mineral.* **101**, 690–705 (2016).

Acknowledgments: We thank J. A. Axler, D. M. Rye, M. Brandon, D. A. D. Evans, and E. M. Stewart for helpful discussions; J. O. Eckert Jr. for EPMA assistance; Z. Jiang for EBSD assistance; and K. K. M. Lee for access to Raman spectroscopy resources. Two anonymous reviewers provided thorough and constructive comments. **Funding:** This work was supported by the U.S. National Science Foundation Directorate of Geosciences (EAR-0744154, EAR-1250269, and EAR-1753553) and Yale University. **Author contributions:** D.S.K. and J.J.A. conducted fieldwork. J.J.A. prepared thin sections. D.S.K. characterized and photographed lamellae, performed EBSD and EPMA analyses, and analyzed data. D.S.K. and J.J.A. drafted and edited the manuscript together. **Competing interests:** The authors declare that they have no competing interests. **Data and materials availability:** All data needed to evaluate this work are present in the paper and/or the Supplementary Materials. MATLAB code used to calculate reconstructed formulae, and any additional data related to this paper may be requested from the authors.

Submitted 25 June 2019
Accepted 12 December 2019
Published 13 March 2020
10.1126/sciadv.aay5178

Citation: D. S. Keller, J. J. Ague, Quartz, mica, and amphibole exsolution from majoritic garnet reveals ultra-deep sediment subduction, Appalachian orogen. *Sci. Adv.* **6**, eaay5178 (2020).